Target-oriented least-squares reverse-time migration with Marchenko redatuming and double-focusing
Field data application

Shoja, Aydin ; van der Neut, Joost; Wapenaar, Kees

DOI
10.1190/geo2023-0374.1

Publication date
2024

Document Version
Submitted manuscript

Published in
Geophysics

GEOPHYSICS®

Target-oriented least-squares reverse-time migration with Marchenko redatuming and double-focusing: Field data application

Journal:	*Geophysics*
Manuscript ID	GEO-2023-0374
Manuscript Type:	Technical Paper
Keywords:	least-squares migration, Reverse time migration, reciprocity, datuming, internal multiples
Manuscript Focus Area:	Seismic Migration, Seismic Inversion

Target-oriented least-squares reverse-time migration with Marchenko redatuming and double-focusing: Field data application

(June 21, 2023)

Running head: **Norwegian Sea target-oriented LSRTM**

ABSTRACT

Recently, the focus of reflection seismologists has shifted to applications where a high-resolution image of the subsurface is required. Least-Squares Reverse-Time Migration (LSRTM) is a common tool used to compute such images. Still, its high computational costs have led seismologists to use target-oriented LSRTM for imaging only a small target of interest within a larger subsurface block. Redatuming the data to the upper boundary of the target of interest is one approach to target-oriented LSRTM. Still, many redatuming methods cannot account for multiple scatterings within the overburden. This paper presents a target-oriented least-squares reverse time migration algorithm which integrates Marchenko redatuming and double-focusing. This special redatuming method accounts for all orders of multiple scattering in the overburden for target-oriented LSRTM. Additionally, the paper demonstrates that a double-focusing algorithm can further reduce the size of the data by reducing both spatial and temporal dimensions. This algorithm is applied to field data acquired in the Norwegian

Sea.

INTRODUCTION

Seismic imaging and inversion are a set of techniques used by geophysicists to estimate parameters related to wave propagation, such as reflectivity, velocity, and density, within the Earth's subsurface. A network of sources and receivers is positioned on the Earth's surface to determine these parameters to produce and record seismic waves. Geophysicists typically assume a model of the subsurface that separates into a background model (m_0) for longer wavelengths and a short-wavelength reflectivity model (δm) based on a weak-scattering assumption (Schuster, 2017; Claerbout, 1985). The primary objective of seismic imaging is to generate a structural image of the short-wavelength reflectivity model (δm).

Reverse-Time Migration (RTM) is more popular among different imaging techniques since it can produce higher-resolution images and better handles complex geological structures (Baysal et al., 1983; McMechan, 1983; Zhou et al., 2018; Zhang et al., 2019). RTM creates images by cross-correlating the forward-propagated wavefield and its back-propagated counterpart based on Born approximation. However, improving the resolution and quality of RTM images is still possible by inverting them with a least-squares algorithm (Dutta et al., 2017; Tang, 2009; Liu et al., 2016). This process is known as Least-Squares Reverse-time migration (LSRTM).

However, LSRTM is a computationally expensive algorithm (Dai et al., 2012; Tang, 2009; Herrmann and Li, 2012; Farshad and Chauris, 2021). To reduce the computational cost of LSRTM, one can reduce the model's dimensions by focusing on a small area inside the big block of the subsurface model. To compute the image of this smaller region, the wavefield on the boundary of this region is needed. The process of computing the wavefield on the boundary of this target from surface recorded data is called redatuming (Valenciano et al., 2006; Haffinger et al., 2013; Willemsen et al., 2016; Yuan et al., 2017; Zhao and Sen, 2018; Guo and Alkhalifah, 2020; Ravasi et al., 2016). One prominent redatuming technique is Marchenko redatuming (Wapenaar et al., 2014, 2021; Diekmann and Vasconcelos, 2021).

Marchenko redatuming can create virtual receivers on the boundary of the target of interest while accounting for all orders of internal multiple scatterings and reflections. Since Marchenko redatuming and Green's functions retrieval are powerful tools, researchers use them to address issues in seismic imaging and inversion (Cui et al., 2020; Zhang et al., 2019; Diekmann et al., 2023). Moreover, with Marchenko double-focusing, it is possible to create virtual sources and redatum both sources and receivers to the boundary of the target (Staring et al., 2018; Shoja et al., 2023). Marchenko double-focused wavefields account for all orders of internal multiples generated inside the overburden, enabling us to create images with less impact from internal multiples. Moreover, Marchenko double-focusing compacts the data's time axis, reducing the data's size even more.

This paper combines the Marchenko double-focusing and target-oriented LSRTM algorithm to create high-resolution artifact-free images of a marine data set from the Vøring region in the Norwegian Sea. First, we review the theory of target-oriented LSRTM with Marchenko double-focusing. Second, we apply this algorithm to a marine dataset, and finally, we discuss the results and conclude the paper.

THEORY

Least-squares reverse-time migration

Dai et al. (2012) show that classical RTM can be derived from the Born approximation of seismic reflection data. In the Born approximation, the incident wavefield (P^{inc}) can be represented using the background Green's function. The reflectivity model is expressed as $\delta m = (\frac{1}{c^2} - \frac{1}{c_0^2})$ where c represents the modified velocity. This equation links δm to the scattered data (P^{scat}) through a linear equation (Born et al., 1999; Schuster, 2017; van den Berg, 2021):

$$P^{scat}_{pred}(\mathbf{x}_r, \mathbf{x}_s, \delta m, \omega) = \frac{\omega^2}{\rho_0} \int_V G_0(\mathbf{x}_r, \mathbf{x}, \omega) \delta m(\mathbf{x}) G_0(\mathbf{x}, \mathbf{x}_s, \omega) W(\omega)\, d\mathbf{x}. \tag{1}$$

The integral in Equation 1 is computed throughout the model's volume (V), with ω being the angular frequency and the subscripts "r" and "s" indicating the receiver and source, respectively. This equation can be expressed in an operator format as follows:

$$P^{scat}_{pred}(\mathbf{x}_r, \mathbf{x}_s, \delta m, \omega) = \mathcal{L} \delta m. \tag{2}$$

Here $\mathcal{L}$ is the forward Born operator.

The standard method of reverse-time migration involves obtaining an approximate reflectivity model by taking the adjoint of $\mathcal{L}$ and applying it to the observed scattered data:

$$\delta m^{mig}(\mathbf{x}) = \mathcal{L}^{\dagger} P^{scat}_{obs}. \tag{3}$$

Due to the fact that the adjoint of this kernel is merely an approximation of its inverse, the resolution of the reflectivity model obtained through this process is limited.

To tackle the problem of limited resolution, scholars have adopted a least-squares strategy in which the adjoint operator ($\mathcal{L}^\dagger$) is substituted with a damped least-squares solution, as suggested in references (Marquardt, 1963; Dai et al., 2012; Dutta et al., 2017):

$$\delta m^{mig} = [\mathcal{L}^\dagger \mathcal{L} + \epsilon]^{-1} \mathcal{L}^\dagger P_{obs}^{scat}. \tag{4}$$

Unfortunately, calculating the Hessian matrix ($\mathcal{L}^\dagger \mathcal{L}$) and its inverse is computationally infeasible. As an alternative, an iterative algorithm that minimizes the L2-norm of the discrepancy between the observed and anticipated data is often used to update the reflectivity model:

$$C(\delta m) = \frac{1}{2} \| P_{pred}^{scat}(\delta m) - P_{obs}^{scat} \|_2^2. \tag{5}$$

One potential way to tackle this optimization problem is by utilizing a conjugate gradient algorithm (Nocedal and Wright, 2006). In least-squares reverse-time migration, the background velocity model ($c_0(\mathbf{x})$) is not changed, and only the reflectivity model (δm) is updated, resulting in the Green's functions of Equation 1 being calculated only once. To learn more about least-squares reverse-time migration, please see Schuster (2017).

Marchenko redatuming and double-focusing

Marchenko redatuming is an innovative data-driven technique that can recover the Green's function above the target area's surface, including all orders of multiple-scattered events. This method only requires the reflection response at the surface and a smooth background velocity model of the overburden capable of predicting the direct arrival from the surface to the redatuming level.

To retrieve the Green's functions at the redatuming level, the coupled Marchenko-type representations are solved iteratively, as shown in the following equations (Wapenaar et al., 2014):

$$G^{-}_{Mar}(\mathbf{x}_v, \mathbf{x}_r, \omega) = \int_{\mathcal{D}_{acq}} R(\mathbf{x}_r, \mathbf{x}_s, \omega) f_1^{+}(\mathbf{x}_s, \mathbf{x}_v, \omega)\, d\mathbf{x}_s - f_1^{-}(\mathbf{x}_r, \mathbf{x}_v, \omega), \tag{6}$$

and

$$G^{+}_{Mar}(\mathbf{x}_v, \mathbf{x}_r, \omega) = -\int_{\mathcal{D}_{acq}} R(\mathbf{x}_r, \mathbf{x}_s, \omega) f_1^{-}(\mathbf{x}_s, \mathbf{x}_v, \omega)^{*}\, d\mathbf{x}_s + f_1^{+}(\mathbf{x}_r, \mathbf{x}_v, \omega)^{*}. \tag{7}$$

In these equations, $\mathcal{D}_{acq}$ represents the acquisition surface where $\mathbf{x}_s$ and $\mathbf{x}_r$ are situated. G^{-}_{Mar} and G^{+}_{Mar} denote the up-going and down-going components of the Marchenko redatumed Green's function, respectively (see Fig. 1(a) and 1(b)). Additionally, $f_1^{-}(\mathbf{x}_s, \mathbf{x}_v, \omega)$ and $f_1^{+}(\mathbf{x}_s, \mathbf{x}_v, \omega)$ denote the up-going and down-going parts of the focusing function, respectively, with the subscript "v" denoting a virtual point situated on the redatuming level denoted by $\mathcal{D}_{tar}$. Furthermore, $R(\mathbf{x}_r, \mathbf{x}_s, \omega)$ refers to the dipole response of the medium at the acquisition surface, and it is related to the up-going Green's function (G^{-}) via the following relationship:

$$R(\mathbf{x}_r, \mathbf{x}_s, \omega) = \frac{\partial_{3,s} G^{-}(\mathbf{x}_r, \mathbf{x}_s, \omega)}{\frac{1}{2} i\omega\rho(\mathbf{x}_s)}, \tag{8}$$

The partial derivative in the downward direction taken at $\mathbf{x}_s$ is denoted by $\partial_{3,s}$. It is important to remove horizontally propagating waves and surface-related multiples before inserting $R(\mathbf{x}_r, \mathbf{x}_s, \omega)$ into Equations 6 and 7. The detailed derivation of these integrals and their solution for computing the focusing functions and Green's functions can be found in Wapenaar et al. (2014) and Thorbecke et al. (2017).

The above-mentioned equations correspond to single-sided redatuming. To perform a double-sided redatuming, a convolution operation on the up-going and down-going parts of the Marchenko redatumed Green's function is proposed by Staring et al. (2018). This operation involves filtering the down-going focusing function in a multi-dimensional manner:

$$G_{df}^{-,+}(\mathbf{x}_v, \mathbf{x}_v', \omega) = \int_{\mathcal{D}_{acq}} G_{Mar}^{-}(\mathbf{x}_v, \mathbf{x}_r, \omega) \mathcal{F}_1^{+}(\mathbf{x}_r, \mathbf{x}_v', \omega)\, d\mathbf{x}_r, \tag{9}$$

and

$$G_{df}^{+,+}(\mathbf{x}_v, \mathbf{x}_v', \omega) = \int_{\mathcal{D}_{acq}} G_{Mar}^{+}(\mathbf{x}_v, \mathbf{x}_r, \omega) \mathcal{F}_1^{+}(\mathbf{x}_r, \mathbf{x}_v', \omega)\, d\mathbf{x}_r, \tag{10}$$

where

$$\mathcal{F}_1^{+}(\mathbf{x}_r, \mathbf{x}_v', \omega) = \frac{\partial_{3,r} f_1^{+}(\mathbf{x}_r, \mathbf{x}_v', \omega)}{\frac{1}{2} i\omega\rho(\mathbf{x}_r)}. \tag{11}$$

Here the vertical derivative is taken with respect to $\mathbf{x}_r$. Equations 9 and 10 use superscripts to indicate the direction of propagation at the receiver and source locations, respectively. The term ”*df*” stands for ”double-focused.” This process is referred to as ”Marchenko double-focusing.”

The Marchenko double-focusing technique yields two Green's functions, namely a down-going ($G_{df}^{+,+}$) and an up-going ($G_{df}^{-,+}$) Green's function (fig. 1(c) and 1(d)). The down-going Green's function has a band-limited delta function and interactions between the target and the overburden. $G_{df}^{-,+}$ can be interpreted as the continuation of propagation of $G_{df}^{+,+}$ through the target and recording the up-going part of it at the redatuming level. This up-going wavefield includes interactions between the target and the overburden on the source side. In contrast, the conventional double-focusing approach involves using the inverse of the direct arrival of the transmission response of the overburden instead of the down-going Marchenko focusing function. However, this approach cannot predict and remove the multiples generated by the overburden. In the subsequent sections, the term "double-focusing" is a general term that refers to both methods, and it is explicitly mentioned where a distinction between the methods is necessary.

[Figure 1 about here.]

Target-oriented LSRTM by Marchenko double-focusing

The following integral is the base for target-oriented LSRTM by Marchenko double-focusing:

$$\hat{P}_{pred}^{scat}(\mathbf{x}'_{vr}, \mathbf{x}'_{vs}, \delta m, \omega) = \frac{\omega^2}{\rho_0} \int_{\nu} \hat{G}_0(\mathbf{x}'_{vr}, \mathbf{x}, \omega) \delta m(\mathbf{x}) P_{df}^{inc}(\mathbf{x}, \mathbf{x}'_{vs}, \omega) d\mathbf{x}. \tag{12}$$

Here, ν is the target volume, $\mathbf{x}$ is a point inside the target, and $\mathbf{x}'_{vs}$ and $\mathbf{x}'_{vr}$ are the virtual source and virtual receiver locations on the upper boundary of the target, respectively. Moreover,

$$P_{df}^{inc}(\mathbf{x}, \mathbf{x}'_{vs}, \omega) = \int_{\mathcal{D}_{tar}} \frac{\partial_{3,vs} G_0(\mathbf{x}, \mathbf{x}_{vs}, \omega)}{\frac{1}{2} i\omega\rho(\mathbf{x}_{vs})} G_{df}^{+,+}(\mathbf{x}_{vs}, \mathbf{x}'_{vs}, \omega) W(\omega)\, d\mathbf{x}_{vs}, \tag{13}$$

and

$$\hat{G}_0(\mathbf{x}'_{vr}, \mathbf{x}, \omega) = \int_{\mathcal{D}_{tar}} \Gamma(\mathbf{x}'_{vr}, \mathbf{x}_{vr}, \omega) G_0(\mathbf{x}_{vr}, \mathbf{x}, \omega)\, d\mathbf{x}_{vr}, \tag{14}$$

where $\Gamma(\mathbf{x}'_{vr}, \mathbf{x}_{vr}, \omega)$ is a point-spread function, which acts as a band limitation filter on the predicted data. For a complete derivation of the above equations and the definition of the point-spread function ($\Gamma(\mathbf{x}'_{vr}, \mathbf{x}_{vr}, \omega)$), we refer to Shoja et al. (2023). Thus, the new cost function is:

$$C(\delta m) = \frac{1}{2} \| \hat{P}^{scat}_{pred}(\delta m) - \hat{P}^{scat}_{obs} \|^2_2, \tag{15}$$

which we solve with a conjugate gradient algorithm.

FIELD DATA EXAMPLE

Field data explanation

This part of the paper shows the results of the Marchenko-based target-oriented LSRTM on a field dataset provided by Equinor, which was acquired in the Norwegian Sea in 1994. The depth of the water bottom is $1.5km$, which is deep enough to separate the free-surface multiple reflections from the primary and internal multiple reflections. The field dataset contains 399 shot gathers with 180 traces per gather, and the spatial sampling of sources and receivers is $25m$. The field dataset was processed according to Davydenko and Verschuur (2018a) methodology, which involved muting the direct wave, estimating near-offset traces through the parabolic Radon transform (Kabir and Verschuur, 1995), compensating for 3D effects by multiplying with $\sqrt{t}$, and deconvolving the source wavelet. Source-receiver reciprocity is also applied to create offsets in the positive direction to prepare the dataset for the Estimation of Primaries through the Sparse Inversion (EPSI) method to remove free-surface multiples (van Groenestijn and Verschuur, 2009). After source-receiver reciprocity, each gather contains 371 receivers. Table 1 shows the acquisition parameters of this dataset. We apply a gain of $1.73e^{1.3t}$ to the reflection response as recommended by Brackenhoff et al. (2019) to compensate for the absorption effect. However, with this scaling function, the Marchenko redatuming procedure does not sufficiently reduce the multiple reflections energy for imaging. A wrong scaling function can result in more artifacts (van der Neut et al., 2015a). Thus, we multiplied the reflection response already scaled with the aforementioned scaling function, with a range of values to adjust it for imaging. Then, we measured the L2-norm of the double-focused gather to find the value which produces the minimum energy (van der Neut et al., 2015b; Brackenhoff, 2016). Figure 2 shows the L2 norm of the double-focused gather against the values we use. According to Figure 2, we choose value 10, which results in an adjusted scaling factor of $17.3e^{1.3t}$ for a non-scaled reflection response.

[Figure 2 about here.]

[Table 1 about here.]

Figure 3 shows the surface reflection response after preprocessing, with a source located at $\mathbf{x}_s = (5000m, 0m)$. A Ricker wavelet with a dominant frequency of $30Hz$

is convolved with the data. We choose two different targets inside the medium.

[Figure 3 about here.]

LSRTM with double-focusing

Target of interest 1

Figure 4 shows the smooth velocity model provided by Equinor for migration. The red rectangle inside the velocity model indicates the target area, and the virtual sources and receivers' positions are at the upper boundary of this target area.

[Figure 4 about here.]

We apply the double-focusing algorithm to the field data for this target. For this, we define 241 virtual sources and 241 virtual receivers with a spacing of $12.5m$ at $2500m$ depth extending from $9000m$ to $12000m$ over the upper boundary of the first target area. The up-going wavefield resulting from double-focusing is used as input for LSRTM and is called 'observed data' in the following. Figure 5 shows the observed, and predicted data, and the residuals of Marchenko double-focusing target-oriented LSRTM. Moreover, Figure 6 shows the same but for a conventional double-focusing approach. Conventional means using the inverse of the direct arrival between the target and the surface as the redatuming operator instead of the Marchenko focusing functions. The non-physical noises inside the data are caused by imperfect surface multiple elimination in this part of the data. The computational advantage of target-oriented LSRTM with double-focused data is twofold. First, this algorithm reduces the spatial dimension of the problem, and second, it reduces the temporal dimension of the problem as well. The original recording time of the data at the surface is 8 seconds, whereas the temporal length of the double-focused data is 0.5 seconds.

[Figure 5 about here.]

[Figure 6 about here.]

Figure 7 compares the LSRTM images of using Marchenko and conventional double-focused data as input. Figure 7 shows some improvements from using Marchenko double-focused wavefields compared to conventional double-focused ones. A comparison of our results with the results of Davydenko and Verschuur (2018b) and Ypma and Verschuur (2013) confirms that the suppressed events are likely multiple reflections.

[Figure 7 about here.]

Moreover, Figure 8 compares the RTM and LSRTM images of Marchenko double-focused data as input. The LSRTM algorithm improved the quality of the image.

[Figure 8 about here.]

Target of interest 2

Here we choose another target. This target is located between depths of $2100m$ and $2600m$ and lateral extension from $7000m$ to $10000m$ as shown in Figure 9. Virtual sources and receivers are located at the upper boundary of this target area.

[Figure 9 about here.]

Figure 10 shows the observed, and predicted data, and the residuals of the Marchenko double-focusing approach. Figure 11 shows the same for the conventional double-focusing approach.

[Figure 10 about here.]

[Figure 11 about here.]

Moreover, Figure 12 shows the LSRTM images of the target-oriented algorithm with Marchenko and conventional double-focusing. The black arrows and ellipse indicate the internal multiple reflections that are suppressed by our method. Figure 13 shows the RTM and LSRTM images of the target-oriented algorithm with Marchenko double-focusing. The quality and resolution of the image are increased by the LSRTM algorithm.

[Figure 12 about here.]

[Figure 13 about here.]

DISCUSSION

In section 2 of this paper, we derive a target-oriented LSRTM algorithm based on double-focusing that can significantly reduce the dimensions of the problem, which also reduces the computational costs of the LSRTM algorithm. We also integrate the Marchenko double-focusing algorithm with our target-oriented LSRTM algorithm to reduce the artifacts caused by internal multiple reflections.

To demonstrate the advantages of our proposed algorithm, we applied it to a dataset acquired by Equinor in the Norwegian Sea in 1994. We chose two different target zones. Figures 4 and 9 show our targets of interest embedded in the entire domain of the region. This spatial dimension reduction is to validate the first advantage we mentioned above. Figures 4a, 5a, 9a, and 10a show the double-focused data with a recording duration of $0.5s$, whereas the recording time of the original data is $8s$.

To move forward with our investigation, we showed the imaging results with double-focusing for both targets. Figure 7 compares the imaging results of the conventional and Marchenko double-focusing target-oriented LSRTM. The first panel (fig. 6a) shows the LSRTM result of our proposed algorithm with Marchenko double-focused data, and the second panel (fig. 6b) shows the LSRTM results with conventional double-focused data. Comparing these two panels reveals that using Marchenko wavefields leads to better visualization of true events and fewer artifacts due to internal multiples, delineated by the lines and arrows in those panels. Moreover, Figure 8 shows the resolution and quality improvement of target-oriented LSRTM compared to target-oriented RTM with Marchenko double-focusing.

The same discussion stands for the second target. Figure 12 shows a comparison between conventional and Marchenko double-focusing target-oriented LSRTM images where the internal multiple suppression is visible and indicated by arrows and an ellipse, and Figure 13 shows the RTM and LSRTM images of Marchenko double-focusing target-oriented LSRTM. The quality and resolution of the image are increased noticeably. We use the internal multiple elimination results of Davydenko and Verschuur (2018b) and Ypma and Verschuur (2013) as benchmarks for our results.

CONCLUSION

This paper discusses a target-oriented LSRTM algorithm based on double-focusing. The advantages of this algorithm are: 1) reduction of the spatial dimensions of the problem by choosing a smaller target of interest, and 2) reduction of the temporal dimension of the problem by creating both virtual sources and receivers at the boundary of the target, which leads to lower computational costs. One can also opt for more sophisticated redatuming algorithms such as Marchenko redatuming and double-focusing to create virtual sources and receivers. The advantage of using Marchenko double-focusing compared to a more conventional redatuming algorithm is the ability to predict the internal multiple reflections inside the overburden and a reduction of artifacts due to these multiple reflections.

Present-day seismic imaging and inversion applications need more accurate and higher-resolution images. Computing higher-resolution images demands significant amounts of computational power and time. Thus, devising algorithms that can reduce this computational burden is essential. Our proposed target-oriented algorithm is not only able to greatly reduce the spatial and temporal dimensions of the problem but also can reduce the artifacts due to internal multiple reflections by integrating Marchenko double-focusing with LSRTM algorithm. Consequently, our algorithm enables us to create higher-resolution images with fewer artifacts at a lower computational cost.

REFERENCES

Baysal, E., D. D. Kosloff, and J. W. C. Sherwood, 1983, Reverse time migration: GEOPHYSICS, **48**, 1514–1524.

Born, M., E. Wolf, A. B. Bhatia, P. C. Clemmow, D. Gabor, A. R. Stokes, A. M. Taylor, P. A. Wayman, and W. L. Wilcock, 1999, Principles of optics: Electromagnetic theory of propagation, interference and diffraction of light, 7 ed.: Cambridge University Press.

Brackenhoff, J., 2016, Rescaling of incorrect source strength using marchenko redatuming. (Available at http://resolver.tudelft.nl/uuid:0f0ce3d0-088f-4306-b884-12054c39d5da).

Brackenhoff, J., J. Thorbecke, and K. Wapenaar, 2019, Virtual sources and receivers in the real earth: Considerations for practical applications: Journal of Geophysical Research: Solid Earth, **124**, 11802–11821.

Claerbout, J. F., 1985, Imaging the earth's interior: BlackWell Scientific Publications.

Cui, T., J. Rickett, I. Vasconcelos, and B. Veitch, 2020, Target-oriented full-waveform inversion using Marchenko redatumed wavefields: Geophysical Journal International, **223**, 792–810.

Dai, W., P. Fowler, and G. T. Schuster, 2012, Multi-source least-squares reverse time migration: Geophysical Prospecting, **60**, 681–695.

Davydenko, M., and D. J. Verschuur, 2018a, Including and using internal multiples in closed-loop imaging – field data examples: GEOPHYSICS, **83**, R297–R305.

———, 2018b, Including and using internal multiples in closed-loop imaging - field data examples: GEOPHYSICS, **83**, R297–R305.

Diekmann, L., and I. Vasconcelos, 2021, Focusing and Green's function retrieval in three-dimensional inverse scattering revisited: A single-sided marchenko integral for the full wave field: Phys. Rev. Research, **3**, no. 1, 013206.

Diekmann, L., I. Vasconcelos, and T. van Leeuwen, 2023, A note on Marchenko-linearised full waveform inversion for imaging: Geophysical Journal International, **234**, 228–242.

Dutta, G., M. Giboli, C. Agut, P. Williamson, and G. T. Schuster, 2017, Least-squares reverse time migration with local Radon-based preconditioning: GEOPHYSICS, **82**, S75–S84.

Farshad, M., and H. Chauris, 2021, Sparsity-promoting multiparameter pseudoinverse Born inversion in acoustic media: GEOPHYSICS, **86**, S205–S220.

Guo, Q., and T. Alkhalifah, 2020, Target-oriented waveform redatuming and high-resolution inversion: Role of the overburden: GEOPHYSICS, **85**, R525–R536.

Haffinger, P., A. Gisolf, and P. M. v. d. Berg, 2013, Towards high resolution quantitative subsurface models by full waveform inversion: Geophysical Journal International, **193**, 788–797.

Herrmann, F. J., and X. Li, 2012, Efficient least-squares imaging with sparsity promotion and compressive sensing: Geophysical Prospecting, **60**, 696–712.

Kabir, M. N., and D. Verschuur, 1995, Restoration of missing offsets by parabolic radon transform1: Geophysical Prospecting, **43**, 347–368.

Liu, Y., X. Liu, A. Osen, Y. Shao, H. Hu, and Y. Zheng, 2016, Least-squares reverse time migration using controlled-order multiple reflections: GEOPHYSICS,

81, S347–S357.

Marquardt, D. W., 1963, An algorithm for least-squares estimation of nonlinear parameters: Journal of the Society for Industrial and Applied Mathematics, **11**, 431–441.

McMechan, G. A., 1983, Migration by extrapolation of time-dependent boundary values: Geophysical Prospecting, **31**, 413–420.

Nocedal, J., and S. J. Wright, 2006, Numerical optimization: Springer.

Ravasi, M., I. Vasconcelos, A. Kritski, A. Curtis, C. A. d. C. Filho, and G. A. Meles, 2016, Target-oriented Marchenko imaging of a North Sea field: Geophysical Journal International, **205**, 99–104.

Schuster, G. T., 2017, Seismic inversion: Society of Exploration Geophysicists.

Shoja, A., J. van der Neut, and K. Wapenaar, 2023, Target-oriented least-squares reverse-time migration using Marchenko double-focusing: reducing the artefacts caused by overburden multiples: Geophysical Journal International, **233**, 13–32.

Staring, M., R. Pereira, H. Douma, J. van der Neut, and K. Wapenaar, 2018, Source-receiver Marchenko redatuming on field data using an adaptive double-focusing method: GEOPHYSICS, **83**, S579–S590.

Tang, Y., 2009, Target-oriented wave-equation least-squares migration/inversion with phase-encoded Hessian: GEOPHYSICS, **74**, WCA95–WCA107.

Thorbecke, J. W., E. Slob, J. Brackenhoff, J. van der Neut, and K. Wapenaar, 2017, Implementation of the Marchenko method: GEOPHYSICS, **82**, WB29–WB45.

Valenciano, A. A., B. Biondi, and A. Guitton, 2006, Target-oriented wave-equation inversion: GEOPHYSICS, **71**, A35–A38.

van den Berg, P. M., 2021, Acoustic waves, *in* Forward and Inverse Scattering Algorithms based on Contrast Source Integral Equations: John Wiley & Sons, Ltd, 2, 79–179.

van der Neut, J., I. Vasconcelos, and K. Wapenaar, 2015a, On Green's function retrieval by iterative substitution of the coupled Marchenko equations: Geophysical Journal International, **203**, 792–813.

van der Neut, J., K. Wapenaar, J. Thorbecke, and E. Slob, 2015b, *in* Practical challenges in adaptive Marchenko imaging: 4505–4509.

van Groenestijn, G. J., and D. J. Verschuur, 2009, Estimating primaries by sparse inversion and application to near-offset data reconstruction: GEOPHYSICS, **74**, A23–A28.

Wapenaar, K., J. Brackenhoff, M. Dukalski, G. Meles, C. Reinicke, E. Slob, M. Staring, J. Thorbecke, J. van der Neut, and L. Zhang, 2021, Marchenko redatuming, imaging, and multiple elimination and their mutual relations: GEOPHYSICS, **86**, WC117–WC140.

Wapenaar, K., J. Thorbecke, J. van der Neut, F. Broggini, E. Slob, and R. Snieder, 2014, Marchenko imaging: GEOPHYSICS, **79**, WA39–WA57.

Willemsen, B., A. Malcolm, and W. Lewis, 2016, A numerically exact local solver applied to salt boundary inversion in seismic full-waveform inversion: Geophysical Journal International, **204**, 1703–1720.

Ypma, F., and D. Verschuur, 2013, Estimating primaries by sparse inversion, a generalized approach: Geophysical Prospecting, **61**, 94–108.

Yuan, S., N. Fuji, S. Singh, and D. Borisov, 2017, Localized time-lapse elastic waveform inversion using wavefield injection and extrapolation: 2-D parametric studies: Geophysical Journal International, **209**, 1699–1717.

Zhang, L., J. Thorbecke, K. Wapenaar, and E. Slob, 2019, Transmission compensated primary reflection retrieval in the data domain and consequences for imaging: GEOPHYSICS, **84**, Q27–Q36.

Zhao, Z., and M. K. Sen, 2018, Fast image-domain target-oriented least-squares reverse time migration: GEOPHYSICS, **83**, A81–A86.

Zhou, H.-W., H. Hu, Z. Zou, Y. Wo, and O. Youn, 2018, Reverse time migration: A prospect of seismic imaging methodology: Earth-Science Reviews, **179**, 207–227.

LIST OF FIGURES

1 The Green's functions resulting from Marchenko redatuming and double-focusing. a) down-going part of Marchenko Green's function, b) up-going part of Marchenko Green's function, c) down-going Marchenko double-focused Green's function, and d) up-going Marchenko double-focused Green's function. 25

2 L2 norm of the gather shown in Figure 5a against different scaling values. 26

3 Reflection response with a source located at $\mathbf{x}_s = (5000m, 0m)$ 27

4 The smooth velocity model provided by Equinor for migration. The red rectangle inside the velocity model indicates the first target area. The virtual sources and receivers' positions are at the upper boundary of this target area. 28

5 Marchenko double-focused data with a virtual source located at $\mathbf{x}_{vs} = (10500m, 2500m)$ and virtual receivers at the same depth as virtual sources. a) observed data, b) predicted data after 35 iterations of LSRTM, and c) residuals after 35 iterations of LSRTM. 29

6 Conventional double-focused data with a virtual source located at $\mathbf{x}_{vs} = (10500m, 2500m)$. a) observed data, b) predicted data after 35 iterations of LSRTM, and c) residuals after 35 iterations of LSRTM. 30

7 Comparison of images obtained with Marchenko target-oriented LSRTM (a) and Conventional target-oriented LSRTM (b). Red lines in panel (a) delineate some trends that are not visible in panel (b), and the black arrows and rectangles in panel (b) show some events that may be internal multiple reflection artifacts that are suppressed in panel (a). 31

8 Comparison of images obtained with Marchenko target-oriented RTM (a) and LSRTM (b) of the first target. 32

9 The smooth velocity model provided by Equinor for migration. The red rectangle inside the velocity model indicates the second target area, and the virtual sources and receivers' positions are at the upper boundary. 33

10 Marchenko double-focused data with a virtual source located at $\mathbf{x}_{vs} = (8500m, 2100m)$ and virtual receivers at the same depth as virtual sources. a) observed data, b) predicted data after 35 iterations of LSRTM, and c) residuals after 35 iterations of LSRTM. 34

11 Convetional double-focused data with a virtual source located at $\mathbf{x}_{vs} = (8500m, 2100m)$. a) observed data, b) predicted data after 35 iterations of LSRTM, and c) residuals after 35 iterations of LSRTM. 35

12 Comparison of images obtained with Marchenko target-oriented LSRTM (a) and Conventional target-oriented LSRTM (b). The black arrows and the ellipse in panel (b) indicate some of the internal multiple reflection artifacts that are suppressed in panel (a) 36

13 Comparison of images obtained with Marchenko target-oriented RTM (a) and LSRTM (b) of the second target. 37

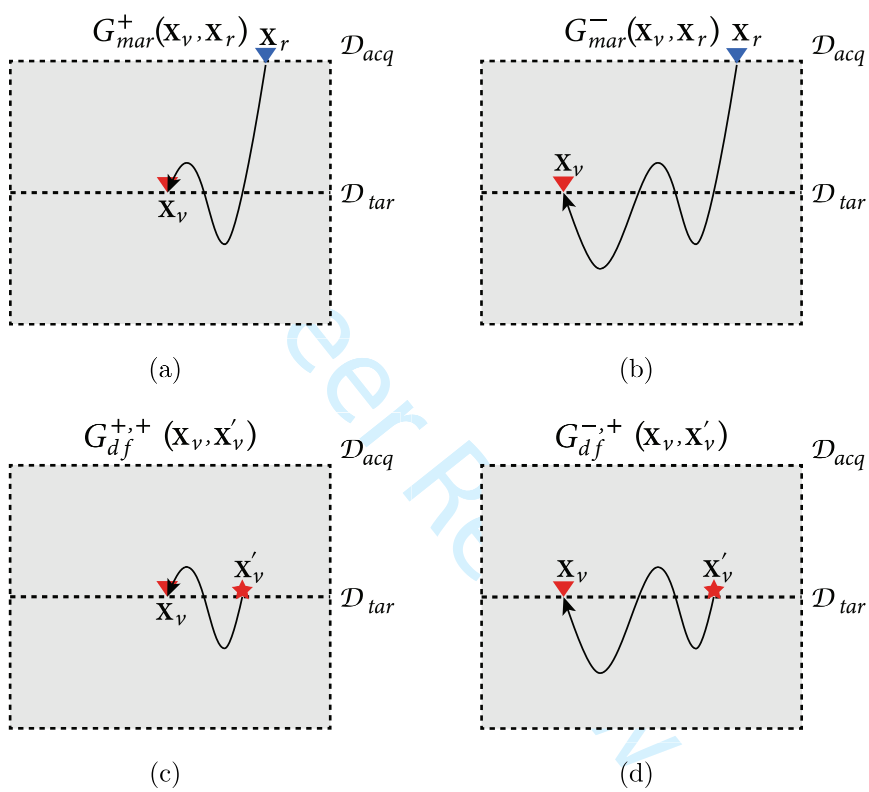

Figure 1: The Green's functions resulting from Marchenko redatuming and double-focusing. a) down-going part of Marchenko Green's function, b) up-going part of Marchenko Green's function, c) down-going Marchenko double-focused Green's function, and d) up-going Marchenko double-focused Green's function.

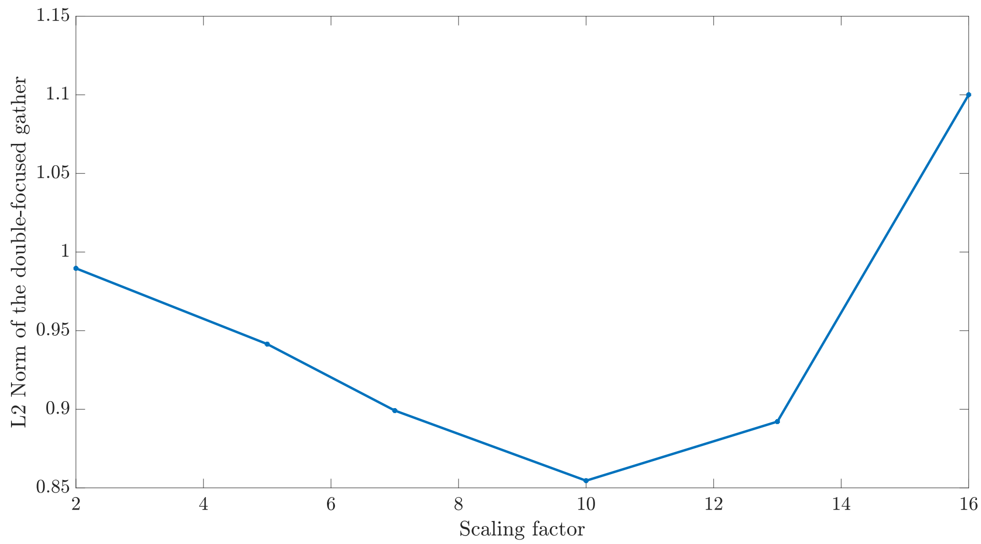

Figure 2: L2 norm of the gather shown in Figure 5a against different scaling values.

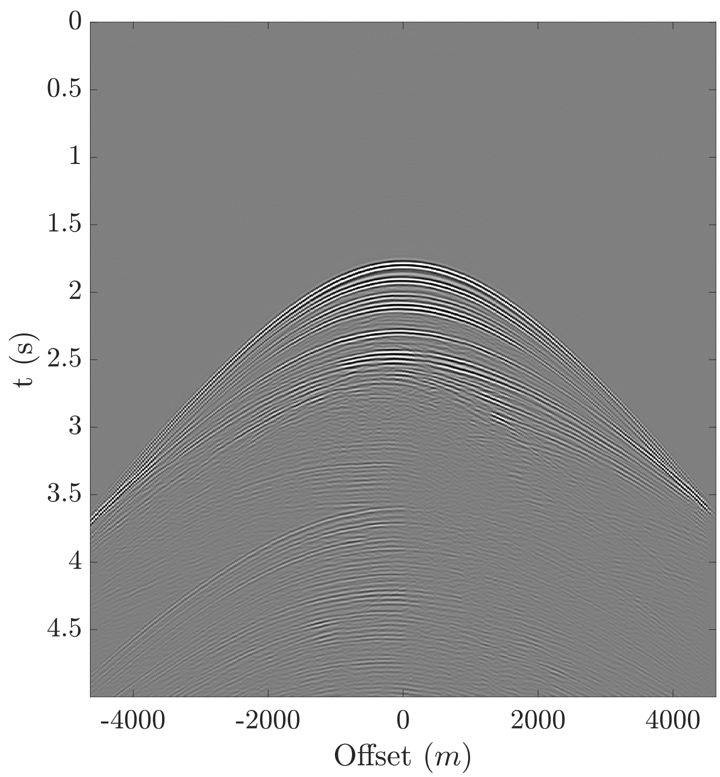

Figure 3: Reflection response with a source located at $\mathbf{x}_s = (5000m, 0m)$

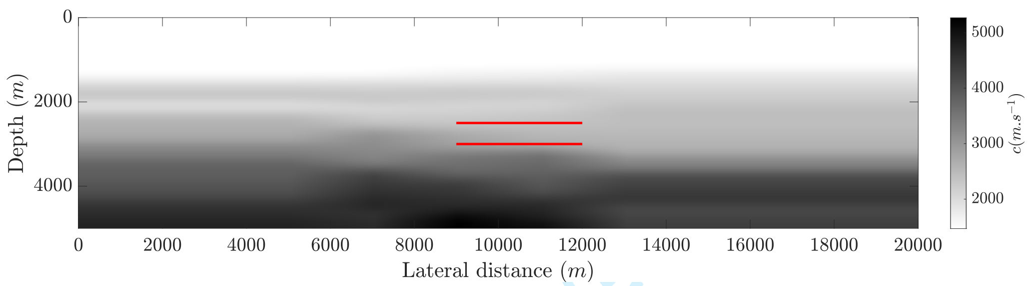

Figure 4: The smooth velocity model provided by Equinor for migration. The red rectangle inside the velocity model indicates the first target area. The virtual sources and receivers' positions are at the upper boundary of this target area.

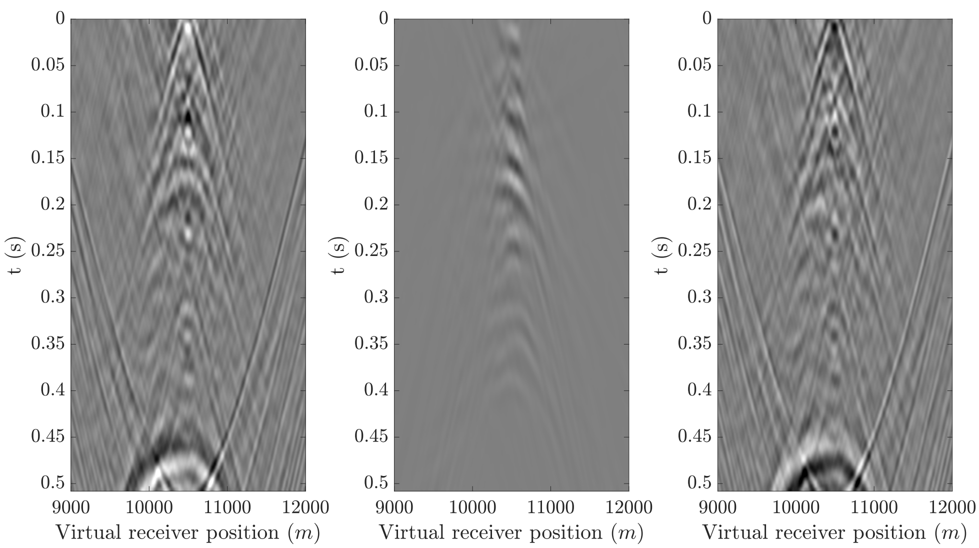

Figure 5: Marchenko double-focused data with a virtual source located at $\mathbf{x}_{vs} = (10500m, 2500m)$ and virtual receivers at the same depth as virtual sources. a) observed data, b) predicted data after 35 iterations of LSRTM, and c) residuals after 35 iterations of LSRTM.

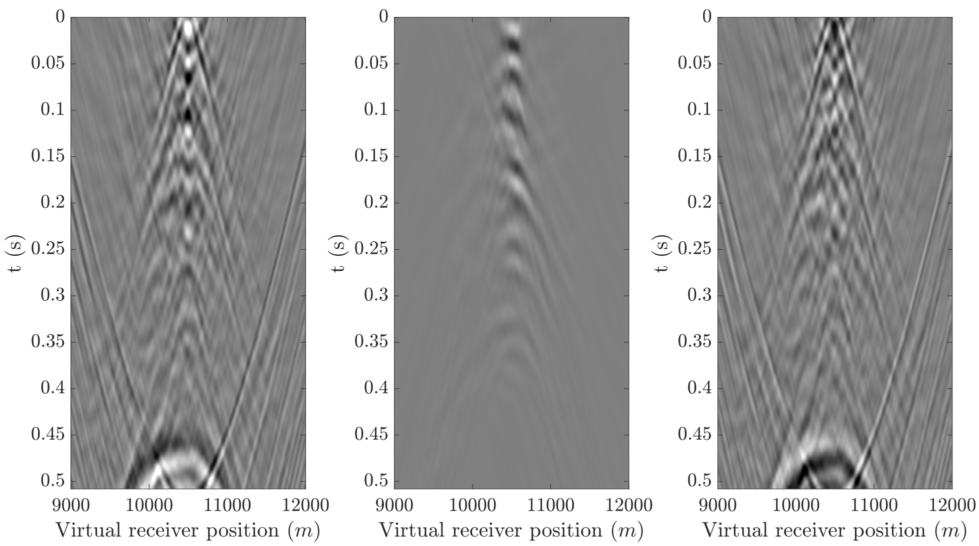

Figure 6: Conventional double-focused data with a virtual source located at $\mathbf{x}_{vs} = (10500m, 2500m)$. a) observed data, b) predicted data after 35 iterations of LSRTM, and c) residuals after 35 iterations of LSRTM.

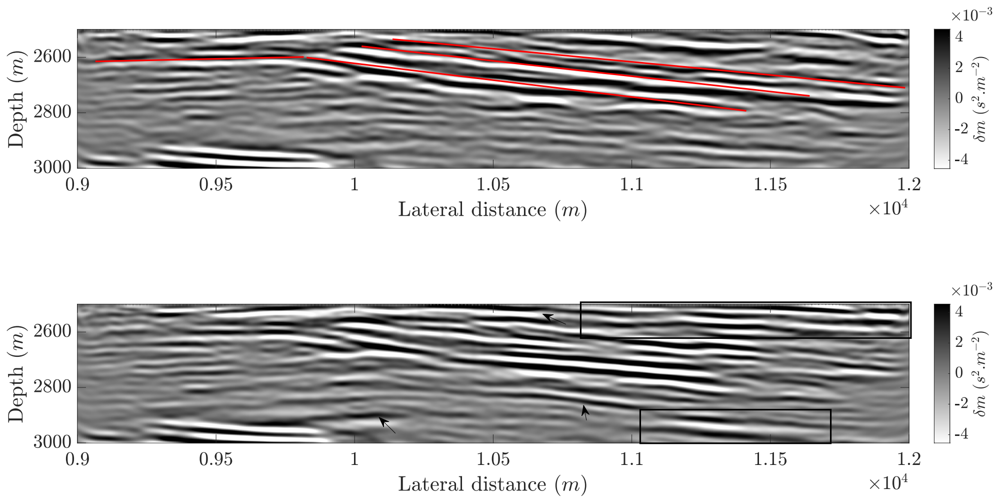

Figure 7: Comparison of images obtained with Marchenko target-oriented LSRTM (a) and Conventional target-oriented LSRTM (b). Red lines in panel (a) delineate some trends that are not visible in panel (b), and the black arrows and rectangles in panel (b) show some events that may be internal multiple reflection artifacts that are suppressed in panel (a).

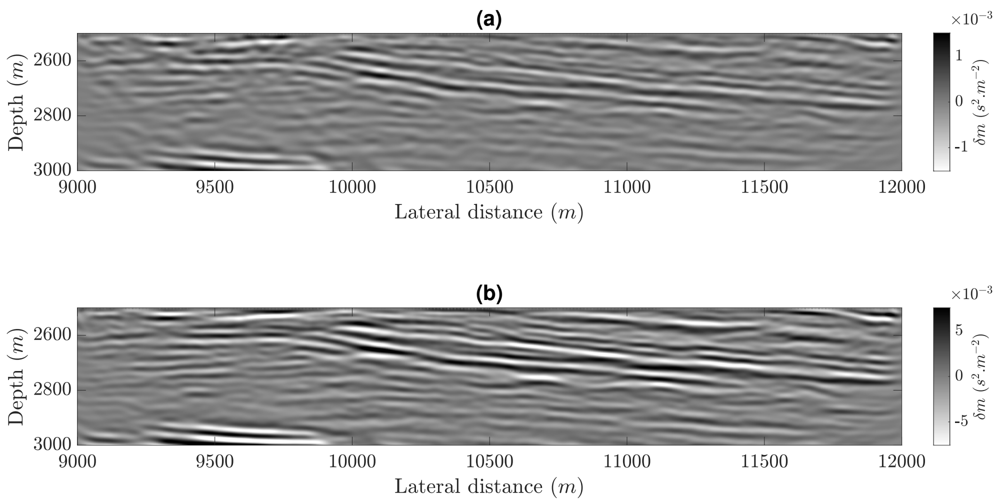

Figure 8: Comparison of images obtained with Marchenko target-oriented RTM (a) and LSRTM (b) of the first target.

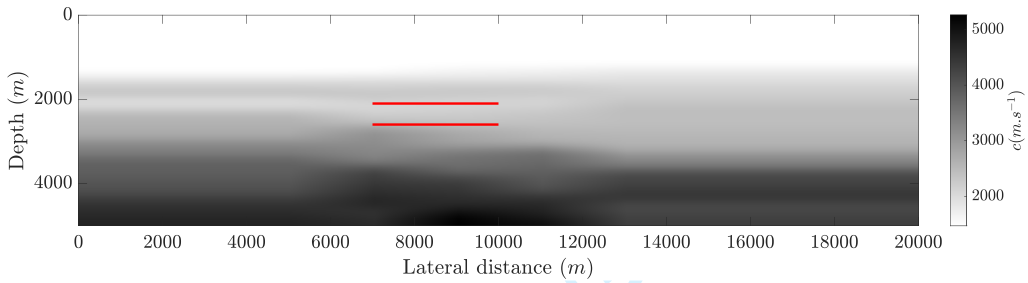

Figure 9: The smooth velocity model provided by Equinor for migration. The red rectangle inside the velocity model indicates the second target area, and the virtual sources and receivers' positions are at the upper boundary.

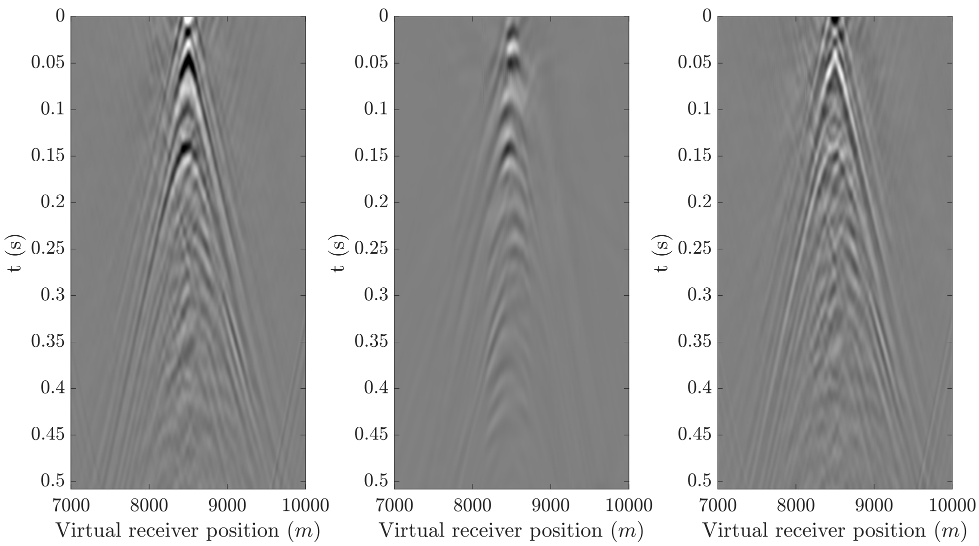

Figure 10: Marchenko double-focused data with a virtual source located at $\mathbf{x}_{vs} = (8500m, 2100m)$ and virtual receivers at the same depth as virtual sources. a) observed data, b) predicted data after 35 iterations of LSRTM, and c) residuals after 35 iterations of LSRTM.

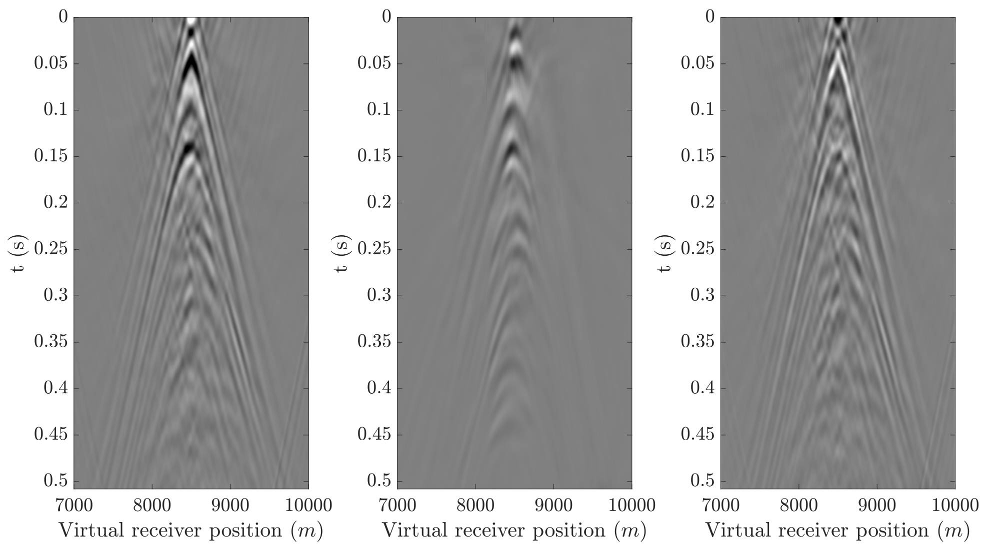

Figure 11: Convetional double-focused data with a virtual source located at $\mathbf{x}_{vs} = (8500m, 2100m)$. a) observed data, b) predicted data after 35 iterations of LSRTM, and c) residuals after 35 iterations of LSRTM.

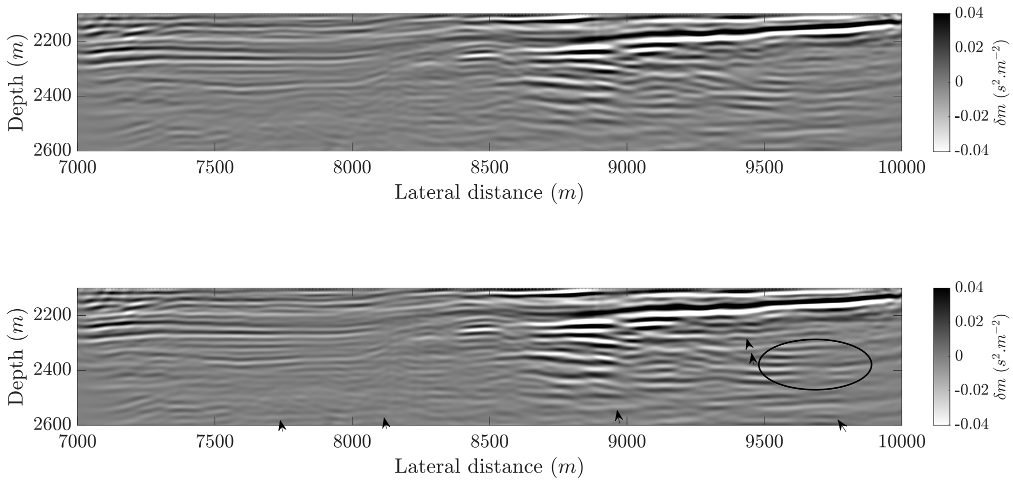

Figure 12: Comparison of images obtained with Marchenko target-oriented LSRTM (a) and Conventional target-oriented LSRTM (b). The black arrows and the ellipse in panel (b) indicate some of the internal multiple reflection artifacts that are suppressed in panel (a)

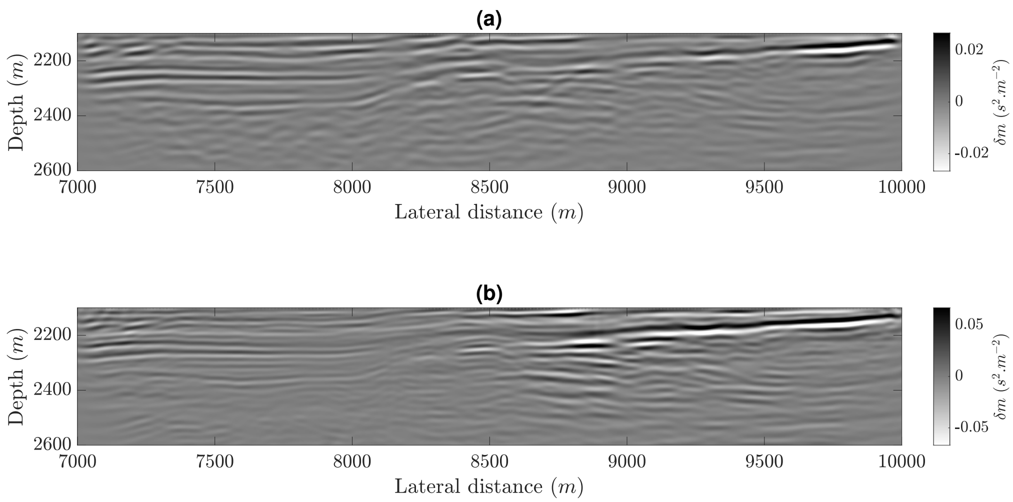

Figure 13: Comparison of images obtained with Marchenko target-oriented RTM (a) and LSRTM (b) of the second target.

LIST OF TABLES

1 Acquisition Parameters for the dataset 39

Parameter	Value
Number of source positions	399
Source spacing	25m
First source position	5,000m
Final source position	14,950
Number of receiver positions per source	180
Receiver spacing	25m
Minimum source-receiver offset	150m
Maximum source-receiver offset	4,625m
Number of time samples	2001
Sampling rate	0.004s
High-cut frequency	90Hz

Table 1: Acquisition Parameters for the dataset